metals

MDPI

Article

Development of a Finite Element Model for the HAZ Temperature Field in Longitudinal Welding of Pipeline Steel

Zhixing Wang, Chengjia Shang * and Xuelin Wang *

Collaborative Innovation Center of Steel Technology, University of Science and Technology Beijing, Beijing 100083, China; jason707165132@163.com
* Correspondence: cjshang@ustb.edu.cn (C.S.); xuelin2076@ustb.edu.cn (X.W.)

Abstract: In this study, a novel hybrid heat source model was developed to simulate the welding temperature field in the heat-affected zone (HAZ) of X80 pipeline steel. This model replicates welding conditions with high accuracy and allows flexible three-dimensional adjustments to suit various scenarios. Its development involved the innovative integration of microstructural crystallography information with a multi-scale calibration and validation methodology. The methodology focused on three critical aspects: the weld interface morphology, the location of the Ac_1 temperature, and the size of prior austenite grains (PAG). The morphology of the weld interface was calibrated to align closely with experimental observations. The model's prediction of the Ac_1 location in actual welded joints exhibited a deviation of less than ±0.3 mm. Furthermore, comparisons of reconstructed PAG sizes between thermal simulation samples and actual HAZ samples revealed minimal discrepancies (5 μm). Validation results confirmed that the calibrated model accurately describes the welding temperature field, with reconstructed PAG size differences between simulation and experimental results being less than 9 μm. These findings validate the accuracy of the calibrated model in predicting welding temperature fields. This research introduces a novel framework for the development of heat source models, offering a robust foundation for improving welding performance and controlling microstructure in different regions during the welding process of high-strength low-alloy (HSLA) steel.

Keywords: heat-affected zone; finite element analysis; hybrid heat source model; microstructural validation; PAG reconstruction

Academic Editor: Jean-Michel Bergheau

Received: 18 December 2024
Revised: 10 January 2025
Accepted: 16 January 2025
Published: 18 January 2025

Citation: Wang, Z.; Shang, C.; Wang, X. Development of a Finite Element Model for the HAZ Temperature Field in Longitudinal Welding of Pipeline Steel. *Metals* **2025**, *15*, 91. https://doi.org/10.3390/met15010091

1. Introduction

Welding plays a pivotal role in the application of steel materials, as it directly impacts the safety and performance of the final products. The microstructure of the heat-affected zone (HAZ), governed by the thermal cycles experienced during welding, is a key factor determining the properties of welded joints, including strength, toughness, ductility, and corrosion resistance [1–5]. With the increasing complexity of modern welding techniques and the ongoing development of high-strength low-alloy (HSLA) steels, engineers and researchers are adopting a variety of design strategies to control and enhance welding performance [6–8]. For instance, in pipeline steels, the demand for thicker plates has led to the widespread use of a two-pass welding process, typically comprising an inner pass followed by an outer pass [9,10]. Among these, the outer pass welding significantly impacts the post-weld properties, as final performance evaluations largely depend on it. The outer pass, governed by the temperature field distribution, results in the formation of the HAZ, which includes the coarse-grained heat-affected zone (coarse-grained HAZ), fine-grained heat-affected zone (fine-grained HAZ), and intercritical heat-affected zone (intercritical HAZ) [11]. Each of these zones exhibits unique widths and microstructural characteristics. Thus, accurately simulating the welding temperature field and extracting thermal cycle characteristics is essential for establishing the relationship between welding processes and the resulting microstructure, with the ultimate goal of controlling the microstructure and distribution of each region.

To analyze the microstructure of welded joints, the traditional approach often involves using the Gleeble system to prepare welding thermal simulation specimens [12,13]. Within this system, the parameters of the welding thermal cycle are computed based on established mathematical models [14]. Commonly utilized models include the Hannerz equation, the Rosenthal equation, and Rykalin 2D and 3D equations. However, these models have limitations in their practical applications and, in many cases, cannot accurately reflect or describe the various thermal cycle parameters [15]. Consequently, samples prepared using the Gleeble system loaded with these models may not accurately replicate the microstructure characteristics of the actual welding samples. Furthermore, this traditional approach heavily depends on trial-and-error methodologies, which are both inefficient and costly. Advances in computational technologies have enabled a shift from analytical equation-based methods to numerical modeling for calculating welding temperature fields. Among these approaches, finite element analysis (FEA) has been shown to provide simulation results more aligned with experimental observations. For instance, finite element (FE) models predict weld pool dimensions with far greater accuracy than the Rosenthal model [16]. Recognizing the high accuracy of FEA, researchers have extensively developed heat source models over the years. These models have evolved from simple point heat sources to more sophisticated configurations, such as linear, circular, and complex volumetric models. Presently, commercial welding simulation software typically incorporates three widely recognized heat source models: the Gaussian surface heat source model [17], Goldak’s double ellipsoid heat source model [18], and the conical heat source model [19]. These advancements have significantly enhanced the fidelity of simulation results when compared with experimental data.

However, achieving a good match between the weld interface morphology of actual welded joints and FEA simulations often cannot be accomplished through adjustments to a single heat source model. The widely used heat source models still have limitations in accurately describing key parameters of the temperature field, indicating significant potential for improvement. At the same time, in previous studies, validation methods for assessing the accuracy of heat source models in representing temperature fields have been relatively limited, primarily relying on comparisons of weld interface morphology between FEA simulations and experimental observations of actual welded joints [20,21]. These validation methods are insufficient to fully ensure the accuracy of simulated welding temperature fields across the entire welded joint. For example, temperature monitoring devices, such as thermocouples, may be affected by factors like high temperatures and radiation, leading to measurement errors that compromise the reliability of the validation process [22,23].

In this study, a novel hybrid heat source model was developed to focus on the HAZ of the outer pass welding in longitudinal double-sided submerged arc welding (LDSAW) of X80 pipeline steel. Additionally, a corresponding FE model was established to accurately predict the temperature field during the welding process. To ensure the reliability of the FEA simulations, a novel multi-scale calibration and validation approach based on crystallographic information was adopted. This approach ensures the precise determination of thermal cycle characteristic values, such as the peak temperature (Tp). Notably, the newly developed hybrid heat source model utilizes a multi-layer stacking and coupling approach in three-dimensional space. This design logic allows the heat source model to be customized to suit specific welding conditions, not only for this case but also for a wide range of welding scenarios. Meanwhile, combined with the novel multi-scale calibration and validation approach based on crystallographic information, it ensures that the hybrid heat source model can reliably and realistically replicate welding temperature fields. By achieving these objectives, this research proposes a novel framework for the development of heat source models, providing a robust foundation for optimizing welding performance and exploring microstructural control in different regions during the welding process of high-strength low-alloy (HSLA) steel.

2. Materials and Methods

In this study, X80 pipeline steel with a thickness of 22.5 mm was used, and its chemical composition and transformation temperatures (Ac_1 and Ac_3) are detailed in Table 1. The critical temperature Ac_1 and Ac_3 was calculated using JMatPro software (v12.1), based on the chemical composition of the X80 pipeline steel used in this study. Material property parameters for the FE model were also derived using JMatPro, ensuring reliable input data. The FE model was developed in Abaqus/CAE, incorporating a newly developed hybrid heat source model implemented in Fortran. The material properties used in the FEA are presented in the Appendix A. The welding process employed a four-wire technique. Gas-shielded welding was used for the root pass, followed by the first pass for the inner side and the second pass for the outer side. H08MnMoTiB special submerged arc welding wire for pipeline steel was combined with flux SJ102G for welding. The welding process (outer) parameters are listed in Table 2, and the parameters used in the FEA simulations were also based on the actual welding process parameters. After etching the cross-section of the welded joint, the weld bead distribution becomes clearly visible, with the affected regions of the first (inner) and second (outer) welding passes distinctly marked, as shown in Figure 1.

Table 1. Alloy chemistry of steels for FE model calibration and validation (wt.%).

Steels	C	Mn	Si	Ni	Cr	Ac_1 (°C)	Ac_3 (°C)	Nb
Calibration	0.05	1.7	0.2	0.15	0.25	831	880	-
Validation (Steel 1)	0.05	1.7	0.2	0.15	0.25	-	-	0.058
Validation (Steel 2)	0.05	1.7	0.2	0.15	0.25	-	-	0.091

Table 2. Welding parameters.

Current (A)	Voltage (V)	Polarity	Diameter (mm)	Heat-Input (kJ/cm)	Speed (m/min)
1000	33	DCEP	4.0	9.9	1.7
800	37	AC	4.0	8.9	
700	42	AC	4.0	8.8	
600	42	AC	3.5	7.6	
Welding parameters ranges			Current: ±10%; Voltage: ±7%; Speed: ±10%; Heat input: ±10%.		

A Gleeble 3500 thermo-mechanical simulator (GTC, Dynamic Systems Inc., Poestenkill, NY, USA) was used for the thermal simulation experiments, with the temperature field obtained from the FE model serving as the input. Samples for microstructure characterization were sectioned, mounted, and mechanically polished following standard metallographic procedures. The polished specimens for scanning electron microscopy (SEM, TESCAN, Brno, Czech Republic) analysis were etched with a solution of nitric acid and alcohol

(1:9) for 7–10 s to reveal the microstructures at various locations in the HAZ. Electron back-scattered diffraction (EBSD, Oxford Instruments, Oxford, UK) analysis was employed for both actual welded joints and thermal simulation samples. The samples were electropolished in a solution of glycerol, perchloric acid, and alcohol (0.5:1:8.5). An acceleration voltage of 20 kV and a step size of 0.15 µm were adopted for EBSD data acquisition. AZtec software (v2.1) was used to determine the PAGs through reconstruction analysis of EBSD data, combined with the Kurdjumov–Sachs (K-S) relationship.

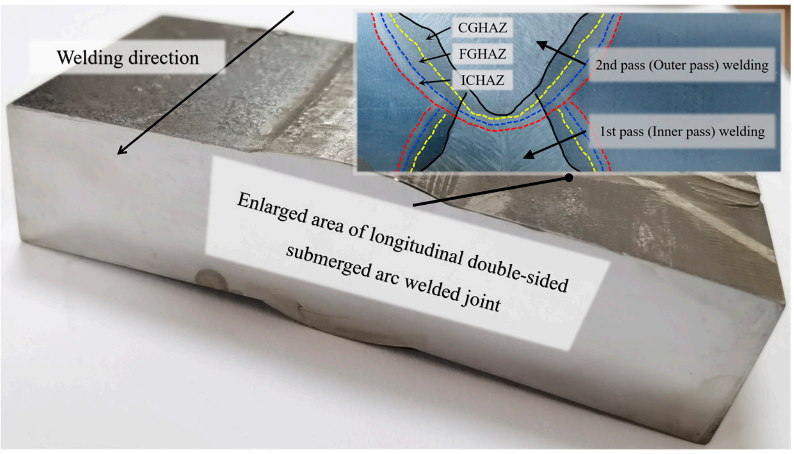

Figure 1. Longitudinal double-sided submerged arc welded joint.

To enhance clarity, a detailed flowchart has been included to illustrate the key steps of the study. The workflow is divided into three main stages, as shown in Figure 2.

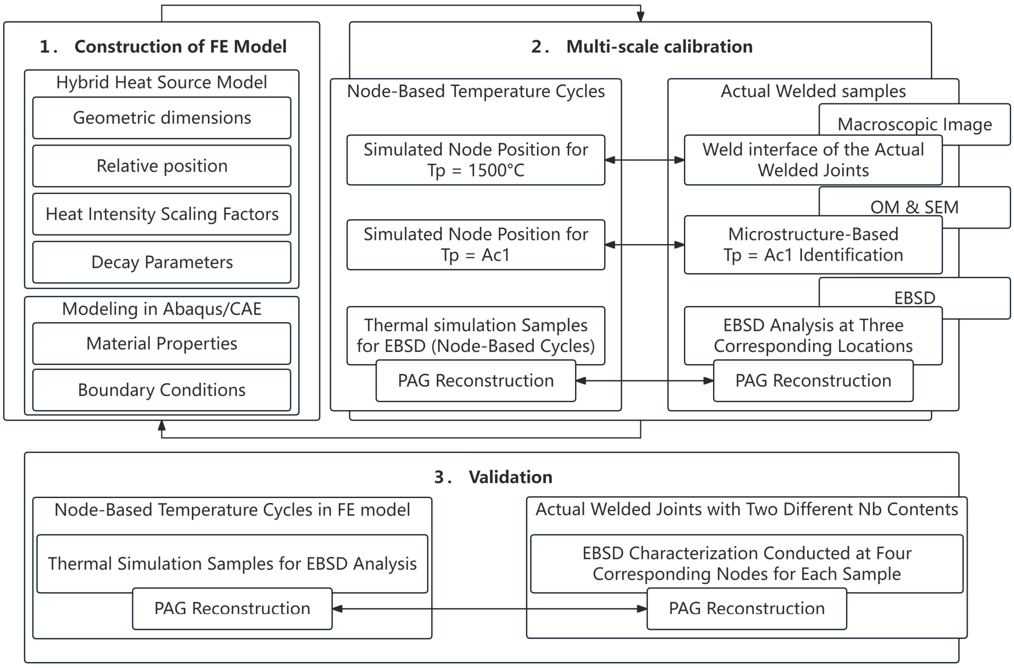

Figure 2. Framework of this study.

The first part of this study involves the construction of the new hybrid heat source and finite element modeling, while the second and third parts introduce a novel multi-scale calibration and validation approach based on crystallographic information. During the calibration process, a single type of steel (referred to as calibration in Table 1) was employed to analyze and collect crystallographic information, such as the SEM and EBSD characterization of the microstructure in the HAZ and PAG reconstruction, which was subsequently used to calibrate the heat source model. The third part focuses on validating the accuracy of the FE model in simulating the HAZ temperature field. To validate the accuracy of the FE model in simulating the HAZ temperature field, two types of X80 pipeline steel (referred to as Steel 1 and Steel 2 in Table 1) were selected for both thermal simulation and actual welding experiments. The two steels differed only in their niobium (Nb) content, while all other elemental compositions remained identical. This selection was made because the growth of austenite is determined by both the material composition and the thermal history it experiences. In this study, validation focused on the thermal history, while validation involved testing the model with steels of different chemical compositions. The differences in austenite growth processes due to varying chemical compositions are reflected in the differences in PAG sizes. Nb was specifically chosen as the variable element because it significantly refines PAG morphology, representing crystallographic transformation pathways during welding [24–26]. Through the above processes, the accuracy of the heat source model in describing the welding temperature field can be effectively validated.

3. Modeling and Calibration

To accurately capture the temperature field experienced at various locations within the HAZ during the welding process, a new heat source model was specifically developed for welding simulations. The FE model's accuracy was calibrated through multi-scale verification, based on crystallographic information using actual welded samples.

3.1. Modeling

Since numerical simulations using the FEA for temperature distributions are governed by Fourier's differential equation, the calculations require temperature-dependent values for thermal conductivity, specific heat capacity, and density. Convection and radiation heat transfers are thermodynamic boundary conditions applied to the external surfaces of the solid. These conditions are essential for accurately capturing the heat exchange between the solid and its surrounding environment and for enabling the simulation of welding temperature fields. During the calculation of the welding temperature field, the metal in the weld area undergoes solid–liquid phase transitions, during which latent heat is absorbed during melting and released during solidification. This latent heat significantly affects the results and cannot be neglected. The phase transition is a nonlinear transient thermal analysis problem. In Abaqus temperature field analysis, this issue is addressed by defining the enthalpy (H) of the material as a function of temperature. This is achieved by inputting the temperature-dependent density and specific heat values of the material before and after phase transformation. The finite element algorithm in Abaqus then calculates the enthalpy values as a function of temperature.

$$H = \int \rho C_{\rho}(T)dT, \tag{1}$$

where ρ represents the density of the material and $C_{\rho}(T)$ is the specific heat, which is temperature-dependent. All these boundary conditions are defined within the FE model. For clarity, these data have been included in the Appendix A.

Currently, the double-ellipsoid heat source model, commonly known as Goldak's model, is the most widely adopted heat source model in commercial programs for the numerical analysis of arc welding processes. Introduced by John Goldak in the early 1980s [27], it consists of two ellipsoids arranged perpendicularly to each other and is characterized by two equations, each representing a distinct part of the ellipsoid. For the front segment of the ellipsoid, the equation is:

$$q_f(x,y,z) = \frac{6\sqrt{3}f_f Q}{abc_f\pi\sqrt{\pi}}e^{-3(\frac{x^2}{a^2})}e^{-3(\frac{y^2}{{c_f}^2})}e^{-3(\frac{z^2}{b^2})}, \tag{2}$$

and for the rear segment of the ellipsoid, the equation is:

$$q_r(x,y,z) = \frac{6\sqrt{3}f_r Q}{abc_r\pi\sqrt{\pi}}e^{-3(\frac{x^2}{a^2})}e^{-3(\frac{y^2}{{c_f}^2})}e^{-3(\frac{z^2}{b^2})} \tag{3}$$

This configuration allows the determination of the heat source size in the plane perpendicular to the welding direction. where q_f, q_r represent the volumetric heat flux density in the front and rear parts of the model, respectively, measured in $\mathrm{W/m^3}$. Additionally, a, b, c_f, and c_r correspond to the width, depth, and length of the front and the rear parts of the estimated molten pool. The total heat transferred to the front and back of the ellipsoid is determined by the parameters f_f and f_r, which must satisfy the condition $f_f + f_r = 2$, with the commonly accepted ratio of f_f to f_r being 60:40. The total introduced power, Q, is given by:

$$Q = \eta UI \tag{4}$$

where U, I represent the welding voltage (V) and current (A), respectively, and η denotes the welding heat efficiency. For this study, a value of 0.85 was adopted.

However, it is well recognized that there is no single heat source that can effectively represent all types of welding processes. Even a single volumetric heat source or a simple coupling of surface and volumetric heat sources cannot precisely depict the temperature field of a welding process under varying welding conditions. Therefore, it is necessary to develop a hybrid heat source model that is applicable to process design and adjustments for various welding processes in three dimensions.

Since actual welding in this study employs the LDSAW method with multiple wires, the weld interface morphology does not exhibit a simple distribution. Instead, the weld interface morphology demonstrates a relatively complex pattern. Additionally, due to the relatively high heat input, the penetration depth is significantly extended in the melt direction. Therefore, the rationale for developing the new hybrid heat source model in this study is as follows: Considering the actual geometric morphology of the welded joints, two volumetric heat source models—the double-ellipsoid heat source (Figure 3a) and the Rotary-Gaussian body heat source (Figure 3b)—are employed and stacked in layers along the melt depth direction [28]. The double-ellipsoid heat source model (Equations (2) and (3)) and the Rotary-Gaussian body heat source (Equation (5)) are used to represent the heat source equations for the upper and lower portions, respectively.

$$q(r,z) = \frac{9Q}{\pi r^2 H}\frac{e^3-1}{e^3}exp(-\frac{9r^2}{{r_0}^2\ln(\frac{H}{h})}), \tag{5}$$

The parameter r_0 represents the radius of the heat source, which can be adjusted to control the top size of the heat source in the coupling process. The parameter H is used to djust the depth of penetration in the lower part of the heat source. The shape of the new hybrid heat source is shown in Figure 3c.

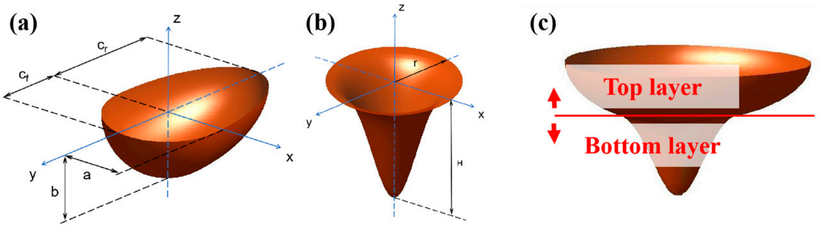

Figure 3. Heat source model and positions for verification. (**a**) Schematic of double-ellipsoid heat source model; (**b**) schematic of Rotary-Gauss body heat source model; (**c**) schematic of new hybrid heat source model.

Since the newly developed heat source model adopts a multi-layer volumetric heat source coupling logic, the net power distribution between the upper and lower heat sources is defined based on their respective contributions. At the same time, the commonly accepted ratio of f_f to f_r in the upper heat source is maintained at 60:40. The upper heat source ($f_f + f_r : 59\%$, $f_f : f_r = 60 : 40$) primarily influences the heat generation within the molten pool, reflecting its dominant role during the initial stages of welding. On the other hand, the lower heat ($f_b\ : 41\%$) source is calibrated to account for heat penetration into the deeper regions of the welded joint, ensuring the accurate representation of the thermal behavior throughout the fusion zone and the HAZ. To ensure the continuity of volumetric heat flux density between the upper and lower heat sources in the hybrid model, a layered coupling approach was employed. The geometric dimensions (a, b, c_f and c_r), relative positions (z and r_0), and scaling factors (f_f, f_r and f_b) were calibrated to align the spatial distribution and intensity of the heat flux in the transition region. The exponential decay parameters were adjusted to ensure smooth overlap between the Gaussian distributions of the upper and lower heat sources.

The FE model was constructed and meshed, utilizing approximately 210,000 elements of the DC3D8 type. The HAZ was meshed with a finer grid compared to other zones in the welded joints to better capture detailed thermal gradients. As shown in Figure 4, three points were selected to verify the temperature field in the transition region from the CGHAZ to the FGHAZ and to ensure that the FE model provides reliable thermal cycle characteristics. The initial temperature of the model was uniformly set to 20 °C, simulating the ambient room temperature before welding. The boundary conditions included a convective heat transfer coefficient of 20×10^{-5} W/mm^2·°C applied to all external surfaces exposed to air, with an ambient temperature of 20 °C, and radiative heat transfer incorporated using an emissivity of 0.06, which is representative of steel surface properties.

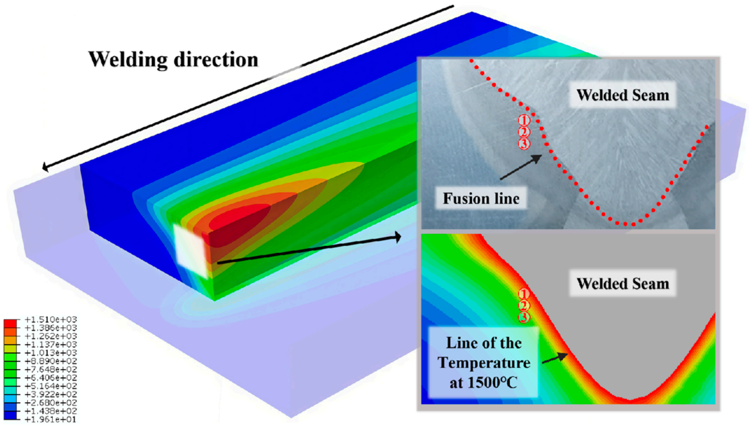

Figure 4. The FE model's temperature field distribution with the positions (1, 2, 3) for the calibration process. The color gradient representing temperature (°C) distribution.

3.2. Multi-Scale Calibration Based on Crystallographic Information

During welding, when the weld seam is heated above the material's melting point, a molten pool is formed. The temperature at the weld interface corresponds to the Tp reached during melting, closely approximating the material's melting point. Using JMatPro software, the solid–liquid transition temperature of the test sample was calculated to determine the Tp of the thermal cycle at the weld interface of the welded joints. This temperature was found to be 1501 ± 11 °C, as shown in Figure 5e. As shown in Figure 5c, the weld interface morphology simulated by the new hybrid heat source model after modification, representing the molten pool shape, was qualitatively compared with experimental observations from the actual welded samples (Figure 5d), showing excellent agreement. In contrast, the classical heat source—Goldak's model—exhibits inevitable deviations from the weld interface of the actual welding samples, even after adjustments, as illustrated in Figure 5d. Therefore, to overcome this limitation, a layered stacking approach was logically adopted in designing the new hybrid heat source model.

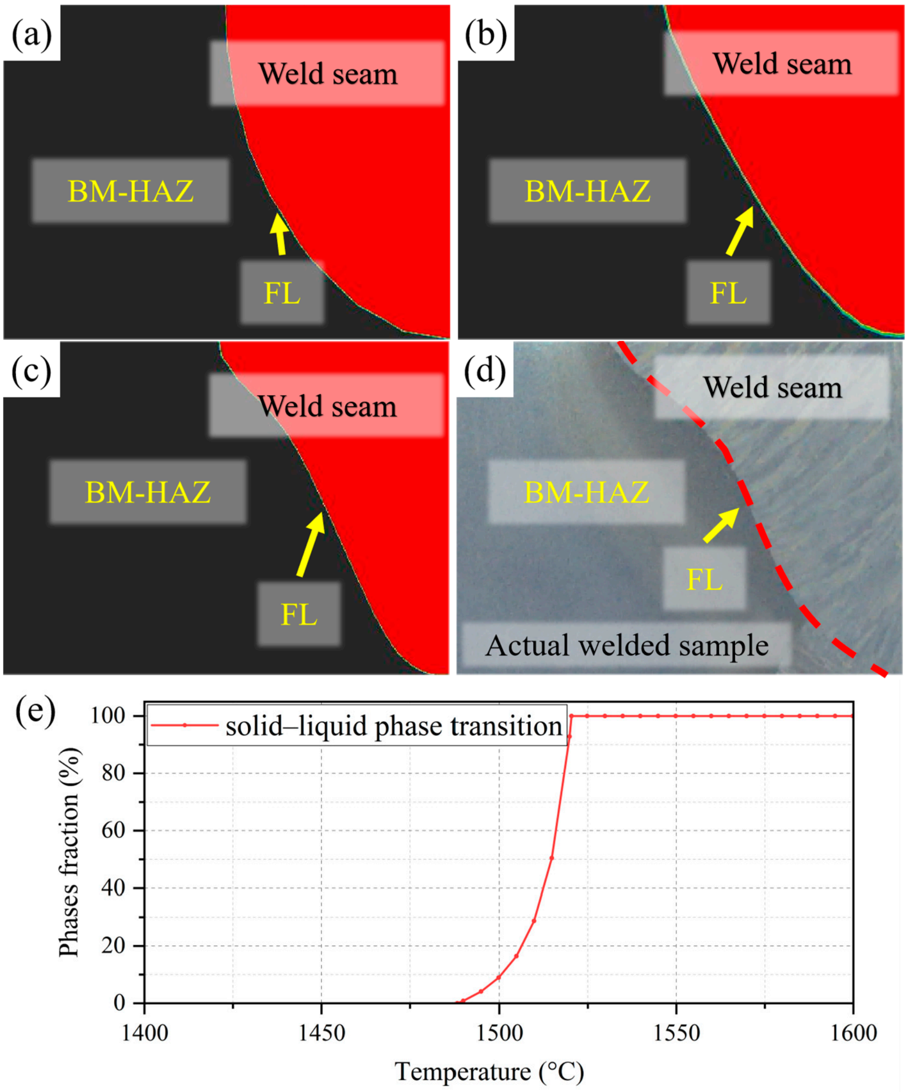

Figure 5. Comparison of weld joints in solid–liquid phase transition with different heat sources. (**a**) Case of Goldak's model; (**b**) case of Rotary-Gauss body heat source model; (**c**) case of new hybrid heat source model; (**d**) welded sample; (**e**) solid–liquid phase transition.

To further calibrate the accuracy of the temperature field obtained from the FE model using the new hybrid heat source, the microstructure in the HAZ of the welding sample was characterized using OM and SEM. These methods were employed to identify the specific positions for temperature cycle verification based on microstructural differences within each region. The locations where the thermal cycle peak temperature (Tp) equaled Ac_1 were employed to calibrate the heat source model. Specifically, the Ac_1 position in the FE model was determined by identifying the Tp in the nodal temperature cycle curve. The Ac_1 position in the actual welded HAZ was identified by comparing the differences in microstructural characterization. As shown in Figure 6c, the microstructure in the intercritical HAZ—formed when the base metal (BM) is heated to temperatures between Ac_1 and Ac_3—contains bainitic ferrite and martensite–austenite (M-A) constituents. In contrast, as shown in Figure 6d, the BM, which is not heated above Ac_1 but still experiences thermal cycling, is influenced primarily by the rolling process and consists of ferrite and bainite [29–31]. By analyzing the microstructural differences between the intercritical HAZ, where the thermal cycle Tp exceeds Ac_1, and the BM, where the Tp remains below Ac_1, it was identified that the region in the actual welded sample influenced by thermal cycling at Tp = Ac_1 is located 4 ± 0.3 mm from the weld interface. After calibration, the simulation results of the heat source model showed that the location of Tp = Ac_1 was identified as 4000 μm from the weld interface, with a discrepancy of less than 0.3 mm compared to the actual welded sample.

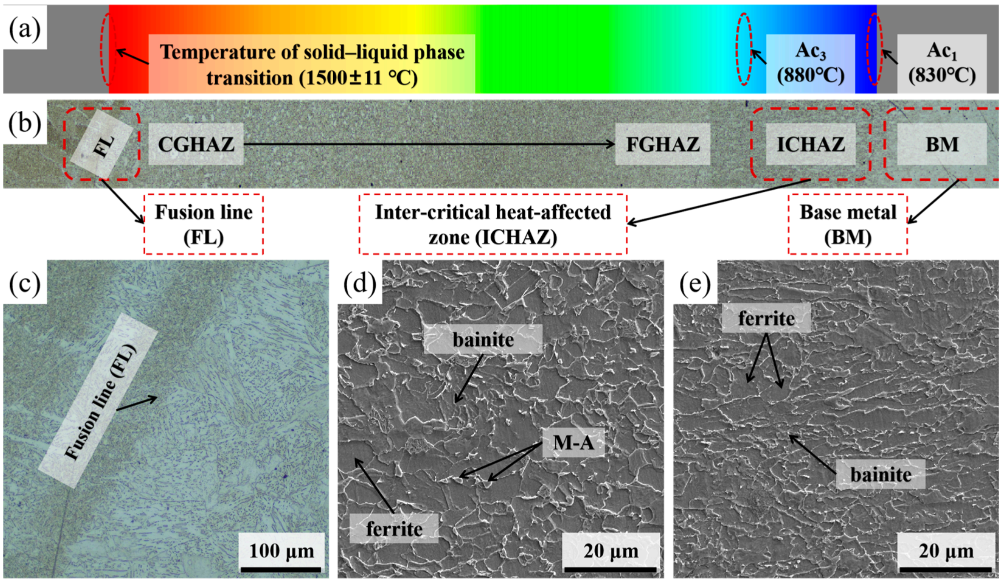

Figure 6. Validation of temperature field in HAZ, (**a**) simulated HAZ; (**b**) OM of HAZ in welded sample; (**c**) OM of weld interface in welded sample; (**d**) SEM of ICHAZ in welded sample; (**e**) SEM of BM in welded sample.

In this research, the verification of the temperature field involved adjustments not only at locations near the heat source (i.e., weld interface) but also at positions farther away (i.e., the Ac_1 locations). Furthermore, as illustrated in Figure 5b, a transitional region exists between the CGHAZ and the FGHAZ, and the heat source model was further refined and calibrated based on this region. During the calibration process, PAG was specifically chosen as the crystallographic characteristic because it serves as a representative feature that encapsulates the crystallographic transformation pathways and the crystal orientations generated during the welding process [32,33]. In the HAZ of the actual welded joint, three positions were selected for EBSD analysis (Figure 4), enabling reconstruction of PAG and statistical measurement of PAG sizes. Similarly, EBSD analysis was performed on the core regions of welding thermal simulation samples affected by thermal cycling to reconstruct PAG and measure PAG sizes. The welding thermal simulation samples were prepared using the Gleeble 3500 thermal simulation system, with thermal cycle curves applied based on the hybrid heat source model at three nodal positions corresponding to the locations selected in the actual welded joint, as shown in Figure 4. The reconstruction of PAG was performed by extracting crystallographic information from EBSD data (e.g., Figure 7(a-1,a-2)) and applying the Kurdjumov–Sachs (K-S) relationship for reconstruction analysis (Figure 7(a-3)). This approach is particularly effective for reconstructing PAG based on crystallographic transformation pathways and crystal orientation [34]. Grain boundary and orientation data were analyzed using AZtec software, generating simulation images and statistical data to describe the morphology of PAG in the HAZ.

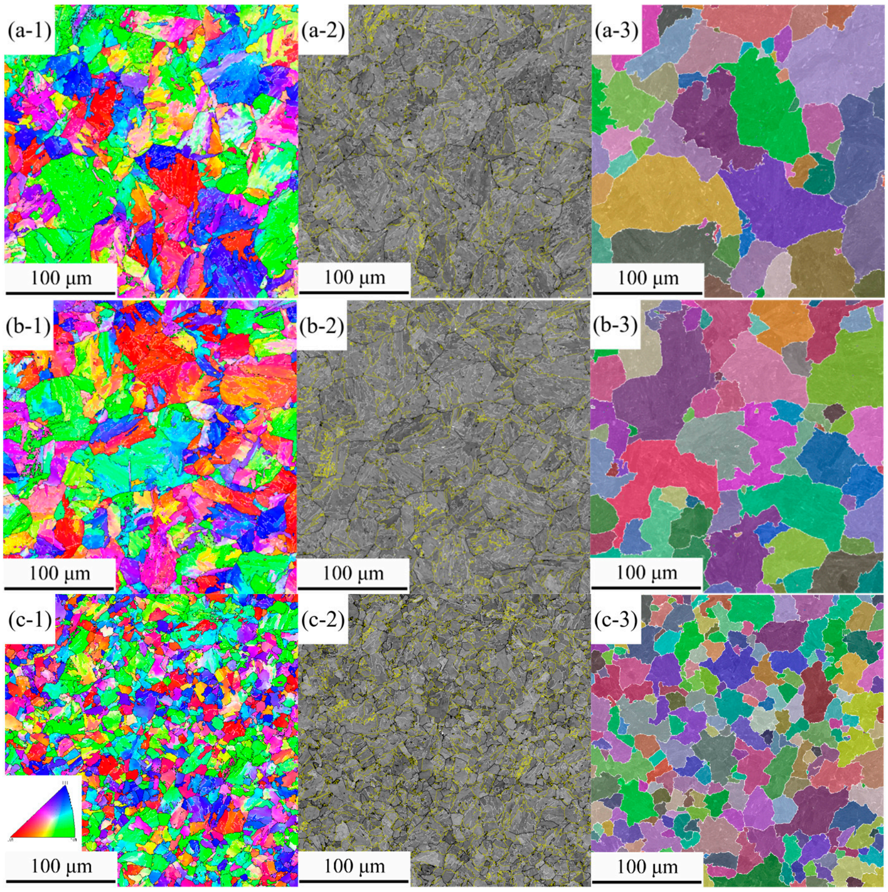

Figure 7. Inverse pole figures, BC images with boundary distributions and the reconstructed PAGs of these samples prepared by thermal simulation, using the temperature field predicted by the FE model, (**a-1**,**a-2**,**b-1**,**b-2**,**c-1**,**c-2**): the EBSD scan results at corresponding position 1, 2 and 3, respectively, (**a-3**,**b-3**,**c-3**): reconstructed PAGs, the different colors represent different grains.

As illustrated in Figure 7, the EBSD scan images of the welding thermal simulation samples include inverse pole figure (IPF) and band contrast (BC) images, providing a detailed visualization of the microstructure. The resulting inverse pole figure (IPF) color map is shown in Figure 7. Different colors represent bainitic crystal units aligned with the observation plane in the vertical direction. The closer the colors, the smaller the orientation difference; conversely, greater color differences indicate larger orientation variations. The analysis indicates that different thermal cycling conditions lead to significant differences in microstructure, primarily in feature size rather than type. Specifically, as the Tp of the thermal cycle increases—corresponding to positions closer to the weld interface in the actual welded sample—both PAGs and bainitic microstructures become finer. Additionally, BC images display the grain boundary distribution, which was analyzed using Channel 5 software. Grain boundaries are marked with lines of different colors to represent distinct misorientation angles: white lines for angles of 5–15°, black lines for 15–45°, and yellow lines for angles above 45°. A comparison of these grain boundary distribution maps reveals a strong correlation between grain boundary morphology and distribution and the simulated welding thermal cycling conditions. Specifically, as the Tp of the thermal cycle decreases, the PAG size increases significantly.

Similarly, Figure 8 presents the PAGs at the corresponding positions in the actual welded joints, with Figure 8(a-3,b-3,c-3) representing PAGs at positions 1, 2, and 3, respectively. Similarly to the trend observed in Figure 7, as the comparison positions shifted from position 1 to position 3 and the Tp of the thermal cycle decreased, the PAG sizes in the samples correspondingly decreased. By comparing the reconstructed PAGs at corresponding positions in Figures 7 and 8, it was found that, after the heat source model was calibrated, the PAG sizes in the thermal simulated samples (loaded with the finite element simulated temperature field) closely matched those at corresponding positions in the actual welded samples. The difference in reconstructed PAG size was less than 5 μm. This indicates that the crystallographic transformation pathways and crystal orientations influenced by the thermal history exhibit a very high degree of similarity, which leads to an excellent match in PAG reconstruction. Furthermore, it demonstrates that the thermal history experienced by the thermal simulated samples is highly consistent with the thermal history at corresponding positions in the actual welded joints.

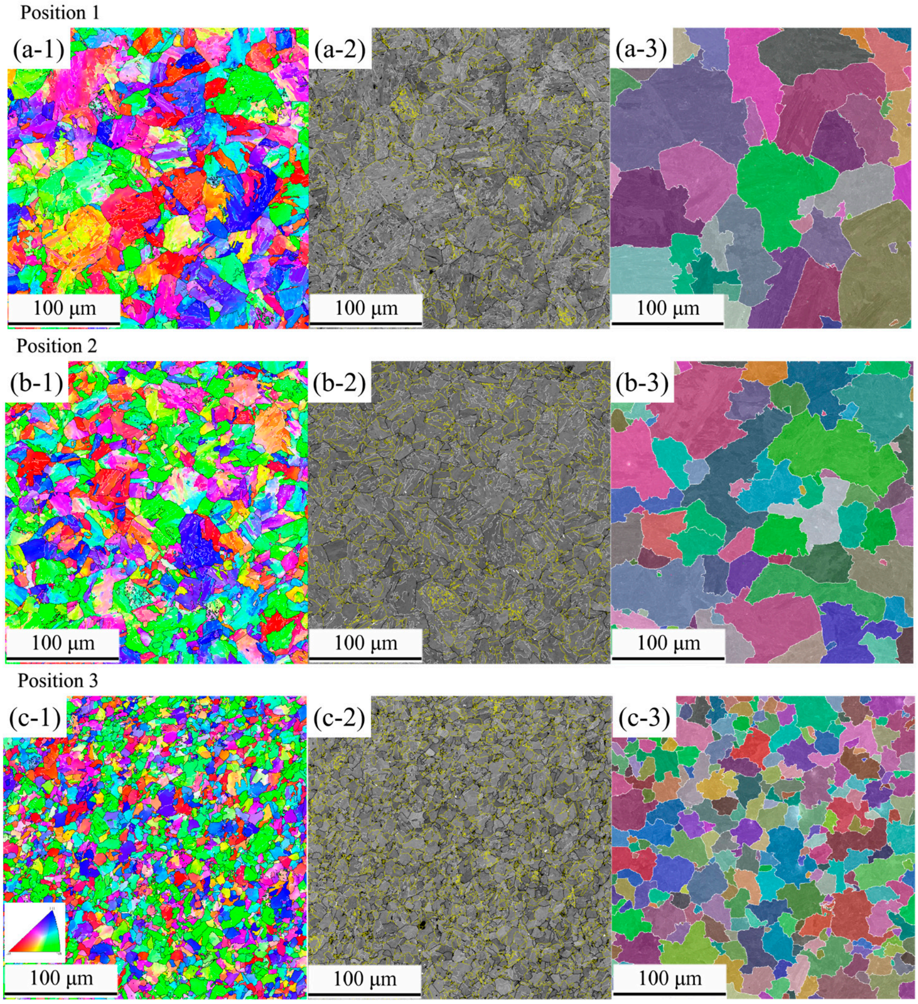

Figure 8. Inverse pole figures, BC images with boundary distributions, and the reconstructed PAGs of actual welded samples, (**a-1**,**a-2**,**b-1**,**b-2**,**c-1**,**c-2**): the EBSD scan results at position 1, 2 and 3, respectively. (**a-3**,**b-3**,**c-3**): reconstructed PAGs, the different colors represent different grains.

The results of the above calibration process demonstrate that the design logic of the newly developed hybrid heat source model allows precise adjustments to specific welding conditions. Additionally, combined with the multi-scale calibration approach based on crystallographic information, it ensures that the hybrid heat source model can reliably and realistically replicate actual welding temperature fields. Additionally, the above results indicate that the simulated temperature field—represented by thermal cycle curves at different positions—can serve as a guide for welding thermal simulation experiments. It can effectively replace the traditional heat source models embedded within the Gleeble system, enabling the preparation of samples that more accurately reflect the microstructural evolution experienced during actual welding processes.

4. Validation and Discussion

To validate the FE model's accuracy in describing the temperature field, two steels with different Nb contents were used to prepare both actual welded samples and Gleeble thermal simulation (FEM-Gleeble) samples. The EBSD analysis and PAG reconstruction were conducted for both actual welded samples and FEM-Gleeble samples. Four HAZ positions (550 μm, 1100 μm, 1650 μm, and 2200 μm from the weld interface, all positioned 3 mm from the top surface of the material) were selected in the actual welded samples for EBSD analysis and PAG reconstruction, followed by the statistical measurement of PAG sizes. Similarly, the FEM-Gleeble samples underwent EBSD analysis and PAG reconstruction, followed by statistical measurement of PAG sizes. In the FEM-Gleeble samples, the thermal cycles applied were derived from the simulation results of four FE model nodes, corresponding one-to-one to the four positions in the actual welded samples (550 μm, 1100 μm, 1650 μm, and 2200 μm from the weld interface). For instance, in Figure 9, a thermal cycle with Tp = 1350 °C corresponds to a location 550 mm outside the weld interface within the HAZ of the actual welded sample.

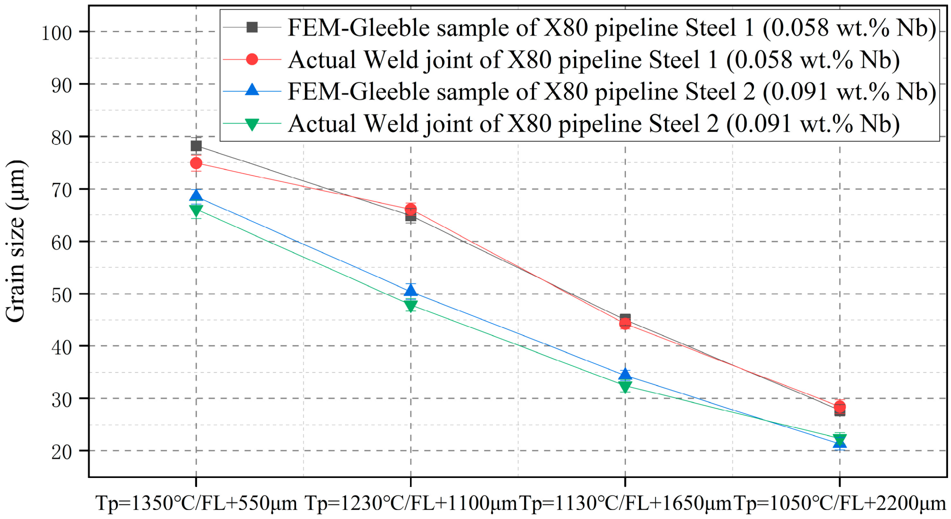

Figure 9. Comparison of the PAG size between simulated samples and actual weld samples.

The growth of austenite is influenced by both material composition and thermal history. In this study, model validation focused on thermal history, while validation involved testing steels with different chemical compositions. The variation in austenite growth processes caused by differences in composition was evaluated based on changes in PAG sizes. Nb was selected as the variable element due to its strong ability to refine PAG morphology, representing crystallographic transformation pathways during welding. During validation, two steels with different Nb contents demonstrated distinct austenite growth behaviors under identical thermal cycling conditions, with the resulting PAG sizes differing based on Nb content. The selected steels were chosen for their varying Nb contents because Nb significantly refines the PAG microstructure through the solute drag effects of Nb and pinning effect of NbC precipitates [35–37].

As shown in Figure 9, samples with different Nb content exhibited significant differences in PAG size under identical thermal cycling conditions, with PAG size decreasing as the Tp of the thermal cycle decreased. Under the same thermal cycling conditions—specifically, at corresponding three-dimensional positions in the FE model and actual welded samples—the PAG sizes in simulated samples closely matched those in actual welded samples, with the largest differences in equivalent circle diameter being less than 9 μm. The morphology of PAG represents the crystallographic transformation pathways and crystal orientations formed during the welding process. The close alignment of reconstructed PAG sizes between thermal simulation and actual welding samples demonstrates the consistency of the thermal cycling conditions influencing these pathways and orientations. This, in turn, validates that the FE model can reliably predict the temperature field during welding.

In summary, the newly developed hybrid heat source, combined with a novel multi-scale calibration and validation approach based on crystallographic information, ensures that the hybrid heat source model can reliably and realistically replicate welding temperature fields. Coupled with the newly developed hybrid heat source model, the established welding FE model can predict temperature fields in various regions of the HAZ, as shown in Figure 10. By achieving these objectives, this research proposes a novel framework for the development of heat source models, providing a robust foundation for optimizing welding performance and exploring microstructural control in different regions during the welding process. Additionally, due to the flexibility of the heat source model, this temperature field prediction model can be adjusted for different welding heat inputs, speeds, and other process parameters to accurately describe the temperature fields experienced by various welding samples. This FE model also guides the process settings for Gleeble thermal simulation equipment, where the applied thermal cycle conditions can effectively replace mathematical models, enabling the Gleeble equipment to produce welding thermal simulation specimens that more accurately reflect actual welding conditions.

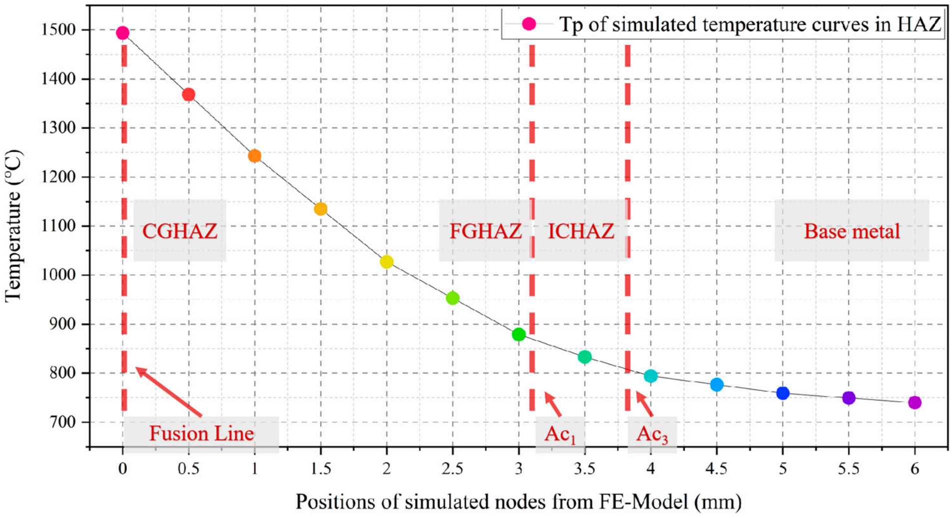

Figure 10. Tp of simulated temperature curves in HAZ.

5. Conclusions

In this study, a newly developed hybrid heat source model was proposed. Additionally, to ensure the reliability of the FEA, a novel multi-scale calibration and validation approach based on actual welding samples was employed. This approach ensures a high level of predictive accuracy for the welding temperature field. The FEA model built upon this framework provides a robust basis for microstructural control in the HAZ and offers substantial support for optimizing welding performance. The findings are summarized as follows:

1. A multi-layer volumetric heat source coupling logic was proposed, enabling the accurate simulation of complex welding scenarios, effectively addressing the limitations of traditional models.
2. An innovative multi-scale calibration and validation approach based on crystallography was developed. This methodology, combining weld interface identification, Ac_1 temperature location, and PAG reconstruction, achieved high accuracy, with results showing deviations within ±0.3 mm for Ac_1 locations and less than 9 μm for PAG size.
3. PAG reconstruction was innovatively applied to validate the welding temperature field, providing detailed insights into thermal cycling effects and confirming the-model's reliability.
4. The heat source model serves as a reliable alternative to traditional thermal simulation methods, producing specimens that accurately represent real welding conditions.

Author Contributions: Conceptualization, Z.W.; data curation, Z.W.; formal analysis, Z.W.; funding acquisition, C.S. and X.W.; investigation, Z.W.; methodology, Z.W. and X.W.; project administration, C.S. and X.W.; resources, C.S. and X.W.; supervision, C.S. and X.W.; validation, Z.W. and X.W.; visualization, Z.W.; writing—original draft, Z.W.; writing—review and editing, Z.W., C.S. and X.W. All authors have read and agreed to the published version of the manuscript.

Funding: This work was funded by the National Natural Science Foundation of China (No. 52271089), the Basic Research and Application Basic Research Foundation of Guangdong Province (No. 2023B1515250006), the Fundamental Research Funds for the Central Universities (No. FRF-BD-23-01), and the Major Scientific and Technological Innovation Project of CITIC Group (No. 2022zxkya06100).

Data Availability Statement: The original contributions presented in this study are included in the article. Further inquiries can be directed to the corresponding authors.

Conflicts of Interest: The authors declare no conflicts of interest.

Appendix A. Material Properties Used in the FEA

As shown in Figure A1, the temperature-dependent thermal material properties used in the FEA are presented in graphical form. These properties include density, thermal conductivity, and specific heat as functions of temperature.

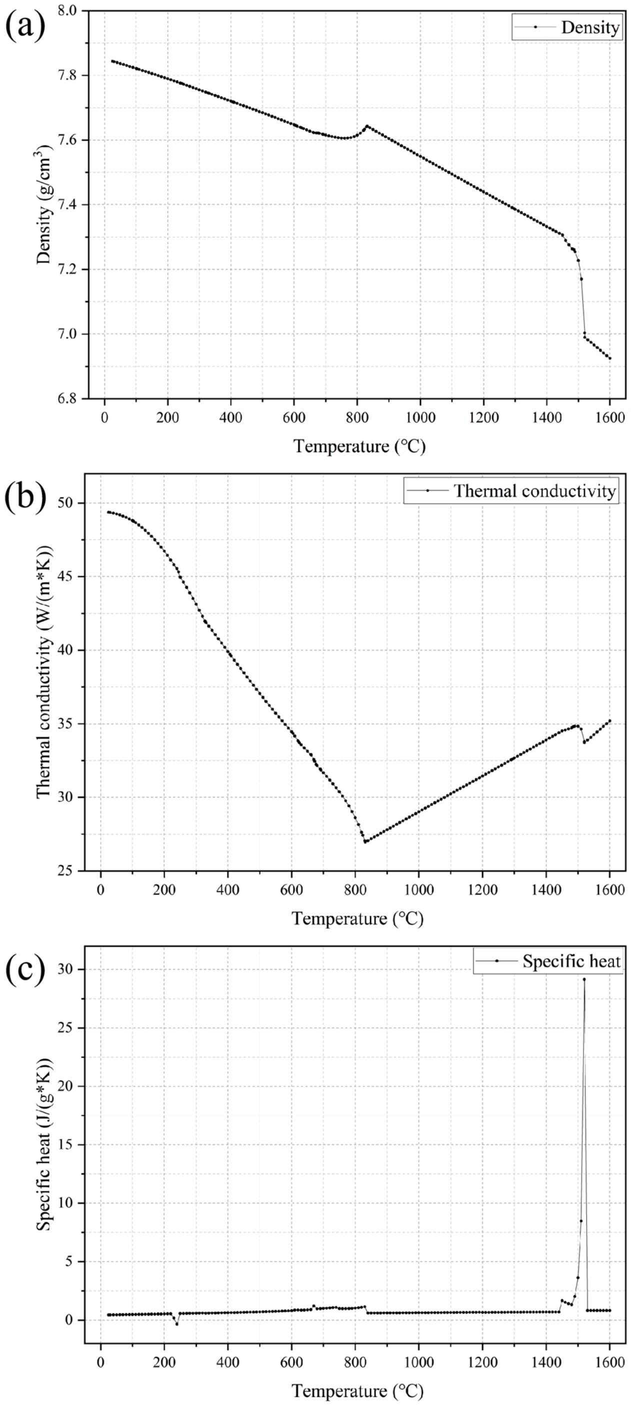

Figure A1. Material properties used in the FEA, (**a**), density; (**b**), thermal conductivity; (**c**), specific heat.

References

1. Yu, Y.; Xu, J.; Chai, T.; Liu, B.; Sun, C. Stress corrosion of HAZ subdivision of X80 pipeline steel in sterile high-sulfate soil. *J. Mater. Res. Technol.* **2023**, *26*, 8229–8241. [CrossRef]
2. Maia, P.P.; Miná, É.M.; Dalpiaz, G.; Marinho, R.R.; Paes, M.T.; Motta, M.F.; de Miranda, H.C.; Silva, C.C. Microstructural characterisation and micromechanical investigation of the heat-affected zone in multi-pass welding of 9Ni steel pipes. *J. Mater. Res. Technol.* **2023**, *24*, 1716–1732. [CrossRef]
3. Jiang, J.; Peng, Z.Y.; Ye, M.; Wang, Y.B.; Wang, X.; Bao, W. Thermal effect of welding on mechanical behavior of high-strength steel. *J. Mater. Civ. Eng.* **2021**, *33*, 04021186. [CrossRef]
4. Bao, L.; Wang, Y.; Han, T. Study on microstructure-toughness relationship in heat affected zone of EQ70 steel by laser-arc hybrid welding. *Mater. Charact.* **2021**, *171*, 110788. [CrossRef]

5. Han, Y.; Fei, J.; Xin, P.; Wang, R.; Jing, H.; Zhao, L.; Xu, L. Microstructure and properties of intercritically reheated coarse-grained heat affected zone in pipeline steel after secondary thermal cycle. *Int. J. Hydrog. Energy* **2021**, *46*, 26445–26456. [CrossRef]
6. Singh, M.P.; Shukla, D.K.; Kumar, R.; Arora, K.S. The structural integrity of high-strength welded pipeline steels: A review. *Int. J. Struct. Integr.* **2021**, *12*, 470–496. [CrossRef]
7. Li, W.; Feng, A.; Wang, Y.; Wang, J. Effect of laser welding parameters on the microstructure and tensile properties of low-alloy high-strength steel. *Mater. Res. Express* **2024**, *11*, 096526. [CrossRef]
8. Meng, X.; Huang, Y.; Cao, J.; Shen, J.; dos Santos, J.F. Recent progress on control strategies for inherent issues in friction stir welding. *Prog. Mater. Sci.* **2021**, *115*, 100706. [CrossRef]
9. Obeid, O.; Leslie, A.J.; Olabi, A.G. Influence of girth welding material on thermal and residual stress fields in welded lined pipes. *Int. J. Press. Vessel. Pip.* **2022**, *200*, 104777. [CrossRef]
10. Sirin, K.; Sirin, S.Y.; Kaluc, E. Influence of the interpass temperature on t8/5 and the mechanical properties of submerged arc welded pipe. *J. Mater. Process. Technol.* **2016**, *238*, 152–159. [CrossRef]
11. Wu, W.; Liu, Z.; Li, X.; Du, C.; Cui, Z. Influence of different heat-affected zone microstructures on the stress corrosion behavior and mechanism of high-strength low-alloy steel in a sulfurated marine atmosphere. *Mater. Sci. Eng. A* **2019**, *759*, 124–141. [CrossRef]
12. da Silva, L.O.P.; Lima, T.N.; Júnior, F.M.D.S.; Callegari, B.; Folle, L.F.; Coelho, R.S. Heat-Affected Zone Microstructural Study via Coupled Numerical/Physical Simulation in Welded Superduplex Stainless Steels. *Crystals* **2024**, *14*, 204. [CrossRef]
13. Afkhami, S.; Javaheri, V.; Amraei, M.; Skriko, T.; Piili, H.; Zhao, X.L.; Björk, T. Thermomechanical simulation of the heat-affected zones in welded ultra-high strength steels: Microstructure and mechanical properties. *Mater. Des.* **2022**, *213*, 110336. [CrossRef]
14. Mičian, M.; Harmaniak, D.; Nový, F.; Winczek, J.; Moravec, J.; Trško, L. Effect of the t 8/5 Cooling Time on the Properties of S960MC Steel in the HAZ of Welded Joints Evaluated by Thermal Physical Simulation. *Metals* **2020**, *10*, 229. [CrossRef]
15. Lee, J. Comparison of Mechanical Properties Between HSS Gleeble Simulated Specimen and Welded Specimen. Bachelor's Thesis, Mechanical Engineering and Production Technology, Riihimäki, Finland, 2022.
16. Hekmatjou, H.; Zeng, Z.; Shen, J.; Oliveira, J.P.; Naffakh-Moosavy, H. A comparative study of analytical Rosenthal, finite element, and experimental approaches in laser welding of AA5456 alloy. *Metals* **2020**, *10*, 436. [CrossRef]
17. Zhou, X.; Wang, Z.-K.; Hu, P.; Liu, M.-B. Discrepancies between Gaussian surface heat source model and ray tracing heat source model for numerical simulation of selective laser melting. *Comput. Mech.* **2023**, *71*, 599–613. [CrossRef]
18. Flint, T.; Francis, J.; Smith, M.; Balakrishnan, J. Extension of the double-ellipsoidal heat source model to narrow-groove and keyhole weld configurations. *J. Mater. Process. Technol.* **2017**, *246*, 123–135. [CrossRef]
19. Jiao, H.; Jin, H. An automated optimization procedure for geometry parameters calibration of two-curvature conical heat source model. *Int. J. Therm. Sci.* **2024**, *197*, 108788. [CrossRef]
20. Giudice, F.; Sili, A. Validation of a theoretical model for laser welding thermal field by multi-physics numerical simulation. *Metals* **2023**, *13*, 2020. [CrossRef]
21. Schauenberg, A.S.; Rodríguez, R.Q.; Almeida, D.T.; Zanon, J.E.; Cunha, E.; Lopes, A.P.; Tonatto, M.L. Evaluating thermal gradient in GMAW welding process with a novel heat source model: Numerical and experimental approach. *Eng. Struct.* **2024**, *318*, 118724. [CrossRef]
22. Zhang, Q.; Ma, H.; Guo, J.; Li, Z.; Xiao, A.; Liu, Y. Analysis of cooling effects and measurement errors in water-cooled thermocouples for total temperature measurement in aviation engine combustion chambers. *Int. J. Therm. Sci.* **2024**, *205*, 109290. [CrossRef]
23. Leonidas, E.; Ayvar-Soberanis, S.; Laalej, H.; Fitzpatrick, S.; Willmott, J.R. A Comparative Review of Thermocouple and Infrared Radiation Temperature Measurement Methods during the Machining of Metals. *Sensors* **2022**, *22*, 4693. [CrossRef]
24. Yang, Y.; Jia, X.; Ma, Y.; Wang, P.; Zhu, F.; Yang, H.; Wang, C.; Wang, S. Effect of Nb on microstructure and mechanical properties between base metal and high heat input coarse-grain HAZ in a Ti-deoxidized low carbon high strength steel. *J. Mater. Res. Technol.* **2022**, *18*, 2399–2412. [CrossRef]
25. Furumai, K.; Wang, X.; Zurob, H.; Phillion, A. Evaluating the effect of the competition between NbC precipitation and grain size evolution on the hot ductility of Nb containing steels. *ISIJ Int.* **2019**, *59*, 1064–1071. [CrossRef]
26. Huang, H.; Yang, G.; Zhao, G.; Mao, X.; Gan, X.; Yin, Q.; Yi, H. Effect of Nb on the microstructure and properties of Ti-Mo microalloyed high-strength ferritic steel. *Mater. Sci. Eng. A* **2018**, *736*, 148–155. [CrossRef]
27. Goldak, J.; Chakravarti, A.; Bibby, M. A new finite element model for welding heat sources. *Metall. Trans. B* **1984**, *15*, 299–305. [CrossRef]
28. Wu, S. A new heat source model in numerical simulation of high energy beam welding. *Trans. China Weld. Inst.* **2004**, *25*, 91–94.
29. Wu, Q.; He, S.; Hu, P.; Liu, Y.; Zhang, Z.; Fan, C.; Fan, R.; Zhong, N. Effect of finish rolling temperature on microstructure and mechanical properties of X80 pipeline steel by on-line quenching. *Mater. Sci. Eng. A* **2023**, *862*, 144496. [CrossRef]
30. Liang, S.; Fazeli, F.; Zurob, H.S. Effects of solutes and temperature on high-temperature deformation and subsequent recovery in hot-rolled low alloy steels. *Mater. Sci. Eng. A* **2019**, *765*, 138324. [CrossRef]

31. Nguyen, V.N.; Nguyen, A.X.; Nguyen, D.T.; Le, H.C. A Comprehensive Understanding of Bainite Phase Transformation Mechanism in TRIP Bainitic-supported Ferrite Steel. *Int. J. Adv. Sci. Eng. Inf. Technol.* **2024**, *14*, 309–325. [CrossRef]
32. Haghdadi, N.; Cizek, P.; Hodgson, P.D.; Tari, V.; Rohrer, G.S.; Beladi, H. Effect of ferrite-to-austenite phase transformation path on the interface crystallographic character distributions in a duplex stainless steel. *Acta Mater.* **2018**, *145*, 196–209. [CrossRef]
33. Wang, X.; Xie, Z.; Li, X.; Shang, C. Recent progress in visualization and digitization of coherent transformation structures and application in high-strength steel. *Int. J. Miner. Metall. Mater.* **2024**, *31*, 1298–1310. [CrossRef]
34. Taylor, M.; Smith, A.D.; Donoghue, J.M.; Burnett, T.L.; Pickering, E.J. In-situ heating-stage EBSD validation of algorithms for prior-austenite grain reconstruction in steel. *Scr. Mater.* **2024**, *242*, 115924. [CrossRef]
35. Zhou, M.; Wang, H.; Zhu, M.; Tian, J.; Su, X.; Zhang, Q.; Guo, A.; Xu, G. New insights to the metallurgical mechanism of niobium in high-carbon pearlitic steels. *J. Mater. Res. Technol.* **2023**, *26*, 1609–1623. [CrossRef]
36. Gong, P.; Palmiere, E.; Rainforth, W. Dissolution and precipitation behaviour in steels microalloyed with niobium during thermomechanical processing. *Acta Mater.* **2015**, *97*, 392–403. [CrossRef]
37. Zeng, Z.; Li, C.; Li, Z.; Zhai, Y.; Wang, J.; Li, Z. Effect of Nb content and thermal deformation on the microstructure and mechanical properties of high-strength anti-seismic rebar. *Mater. Sci. Eng. A* **2022**, *840*, 142929. [CrossRef]